

# Tunable microstructure transformations and auxetic behavior in 3D-printed multiphase composites: The role of inclusion distribution

Jian Li <sup>a</sup>, Stephan Rudykh <sup>b,\*</sup>

<sup>a</sup> Department of Aerospace Engineering, Technion – Israel Institute of Technology, Haifa 32000, Israel

<sup>b</sup> Department of Mechanical Engineering, University of Wisconsin Madison, Madison, WI 53706, USA

## ARTICLE INFO

### Keywords:

Pattern transformation  
Auxetic composite  
3D printing  
Instability

## ABSTRACT

We experimentally and numerically investigate instability-induced pattern transformations and switchable auxetic behavior in multiphase composites consisted of circular voids and stiff inclusions periodically distributed in a soft elastomer. We specifically focus on the role of inclusion distribution on the behavior of the soft transformative composites. The inclusions are distributed in either square or triangular periodic configurations, while the voids are distributed in the triangular periodic array – the configurations enabling cooperative buckling induced transformations of the unit cells. Through the survey of microstructure parameter, we show that tailored positioning of the stiff inclusions can be exploited to expand the set of admissible switchable patterns in multiphase composites. Thus, extreme values of negative Poisson's ratio can be attained through applied strains; moreover, the onset of instabilities, and the corresponding switches to extremely soft behavior are shown to be controlled by the inclusion arrangements and volume fractions. Furthermore, the dependence of the microstructure buckling and post-buckling behavior on loading direction is investigated, and the composite anisotropic properties depending on the microstructure parameters are discussed.

## 1. Introduction

Owing to enhanced mechanical properties and functionalities, microstructured materials – such as, fiber-reinforced or cellular microstructures – have become attractive for various engineering applications [1–6]. The properties tailored through microstructure geometry can be further tuned by external stimuli, or, in case of deformable materials, by pre-stress. In the latter case, the large deformations lead to the evolution in composite microstructures accompanied with geometrical and materials nonlinearities [7–9]. Moreover, the materials may exhibit sudden changes in their microstructures due to elastic instabilities. The phenomenon holds significant potential for designing new materials with switchable properties and functionalities [10–13]. To predict the onset of instabilities and associated buckling modes various techniques have been developed and employed [14–16]; in the context of nonlinear elasticity theory, the framework of small deformation superimposed on the finitely deformed state is used [17]. Within the framework, the onset of macroscopic or long wave instabilities can be predicted through the loss of ellipticity analysis based on the homogenized response of the material [18–23]; while microscopic instabilities can be detected through the Bloch-Floquet analysis [24–29], which also allows to detect

the long wave instabilities for a special limit. In this work, we employ the Bloch-Floquet technique to investigate the instability phenomenon and, then, post-buckling behavior in soft composite with various periodic distributions of voids and stiff inclusions – these structures can exhibit cooperative and controllable collapse of the voids leading to sudden pattern transformations, which hold the potential for responsive and reconfigurable functional materials and devices, such as highly stretchable metamaterials [30], switchable auxetic materials [31], and elastic wave filters [25,32–35], color displays [36], and actuators [37].

Abeyaratne and Triantafyllidis [38] studied the onset of instability in porous solids detecting the loss of ellipticity in homogenized periodic porous elastomer under large strains. Triantafyllidis and Maker [39] examined layered composite with incompressible hyperelastic phases, and showed the connection between the microscopic instability analysis and loss of ellipticity. Geymonat et al. [40] established the rigorous theoretical foundation for Bloch-Floquet technique to detect microscopic and macroscopic instabilities in finitely strained periodic composites; it was shown that the long wave instability limit can be identified with the loss of ellipticity of the homogenized properties. Based on these results, Triantafyllidis et al. [41] numerically

\* Corresponding author.

E-mail address: [rudykh@wisc.edu](mailto:rudykh@wisc.edu) (S. Rudykh).

<https://doi.org/10.1016/j.compositesb.2019.05.012>

Received 7 December 2018; Received in revised form 20 February 2019; Accepted 5 May 2019

Available online 11 May 2019

1359-8368/© 2019 Elsevier Ltd. All rights reserved.

investigated the microscopic and macroscopic instabilities in porous structure with periodic distribution of circular voids. Michel et al. [42] predicted microscopic instabilities in porous system with periodic distribution of circular voids in a square unit cell. The development of the corresponding instability-induced pattern transformations was experimentally observed in an elastomeric system with a square array of circular voids by Mullin et al. [43]. The buckling mode at micrometer length scale were also realized in polymer structures with periodically distributed circular voids fabricated by interference lithography [44–46]. Later, Bertoldi et al. [47] investigated the instability-induced negative Poisson's ratio behavior in the 2D porous systems, and this idea was extended to the design of 3D soft metamaterials with auxetic behavior [48]. In addition, the distribution [49,50] and shape [51,52] of voids were further employed to obtain complex new patterns and to tune Poisson's ratio. Shan et al. [33] employed the anisotropic property of composite structure to trigger multiple pattern transformations in elastomeric porous structure comprising of a triangular periodic arrangement of circular voids. Florijn et al. [53,54] proposed a bi-void system comprising of larger and smaller circular voids to induce co-existing states and switches between these. Overvelde et al. [55] realized the instability-induced checkerboard pattern in soft metamaterial comprising a square array of circular voids under equibiaxial tensile load. Recently, Li et al. [35] introduced the design of switchable soft system comprising of arrays of circular voids and stiff inclusions distributed in a soft matrix. These materials showed new pattern transformations with a strong auxetic behavior.

In this study, we examine the role of the stiff inclusions, their positions and volume fraction, on the instabilities and post-buckling behaviors in the transformative composites; and explore the ways of using this composite design space for tailored performance and enriched instability-induced pattern transformations. Moreover, we examine the multiphase composite anisotropy, and study the response of the composites subjected to different loading directions. First, we discuss possible arrangements of circular stiff inclusions in the structure with periodically distributed circular voids, where new uniform buckling modes are observed. Then, guided by the numerical simulations, we experimentally realize and observe multiple pattern transformations depending on the distribution of inclusions and loading directions in the samples fabricated by multimaterial 3D printing. Next, simulations of infinite periodic and finite size structures are compared with the experimental results of 3D printed samples. Finally, the effect of distribution of stiff inclusions, loading direction, phase volume fraction, and inclusion-to-matrix ratio of shear moduli on the responses of the composites is numerically studied to illustrate the tunability of the systems.

## 2. Specimen design and fabrication, and experimental testing

First, we discuss possible arrangements of circular stiff inclusions in the structure with periodically distributed circular voids. In the periodic

void system a cooperative (or uniform) collapse of the voids happens when the ligaments undergo the same buckling mode simultaneously [50,56]. To achieve this behavior, the geometrical requirements for the void position are: (i) the distance between neighboring voids is identical; (ii) the number of ligaments around each void is an even number. Based on that, we consider two types of distributions of stiff inclusions in the porous structure with circular voids arranged in triangular configuration, while the stiff inclusions are arranged in square (a) and triangular (b) configurations as shown in Fig. 1, which are denoted as *composite type A* and *composite type B*, respectively. The corresponding primitive unit cells are highlighted by light green color.

To investigate the effect of inclusion distribution on the mechanical responses of the proposed anisotropic multiphase composites under different loading directions, the specimens with circular voids and stiff inclusions periodically embedded in an elastomeric soft matrix were fabricated by using a multimaterial 3D printer (Object Connex 260–3). The soft matrix was printed in FLX9860 digital material with initial shear modulus  $\mu^{(m)} = 0.6$  MPa, the stiff inclusion was printed in Vero-White resin with initial shear modulus  $\mu^{(i)} = 600$  MPa. The specimens were characterized with initial volume fraction of soft matrix  $c^{(m)} = 0.25$ , as well as identical void and inclusion radii  $r = 3$  mm. For all specimens, the in-plane dimensions were  $92.37 \times 91.42$  mm (width  $\times$  height), the out-of-plane dimension was  $t = 10$  mm (thickness). In order to track the positions of stiff inclusions during the deformation process, the centroids of stiff inclusions were marked by black dots.

Uniaxial compression tests under plane strain conditions were conducted using the Shimadzu EZ-LX testing machine with maximum load 2 kN. The corresponding experimental setup is shown in Fig. 2. The specimen was held between two transparent parallel fixtures mounted on a metal base to maintain the plane-strain conditions. A plate printed in VeroWhite material and thickness  $t = 10$  mm was placed between the specimen and the testing machine to apply load on the specimen. The compression tests were performed at a constant strain rate of  $4 \times 10^{-4} \text{ s}^{-1}$ . Compression displacement and applied force were recorded to produce stress-strain curves. A high-resolution digital camera was placed in front of the specimen to monitor the deformation process capturing one frame at 0.01 mm compression displacement.

## 3. Numerical modeling

To analyze the mechanical responses for the multiphase composites, numerical simulations are performed for both finite size structure and infinitely periodic structure. The responses of soft matrix and stiff inclusion materials are modeled as neo-Hookean hyperelastic materials, whose strain energy density function is defined as

$$W = \frac{\mu}{2}(I_1 - 3) - \mu \ln J + \frac{\lambda}{2}(\ln J)^2 \quad (1)$$

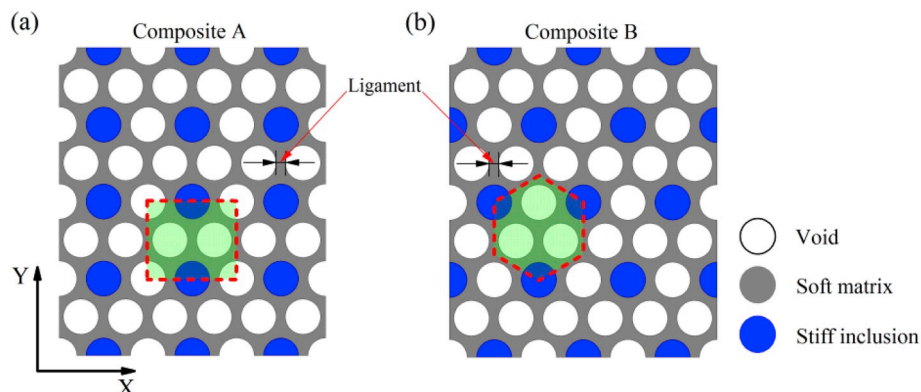


Fig. 1. Schematics of periodic microstructures with circular stiff inclusions arranged in square (a) and triangular (b) configurations.

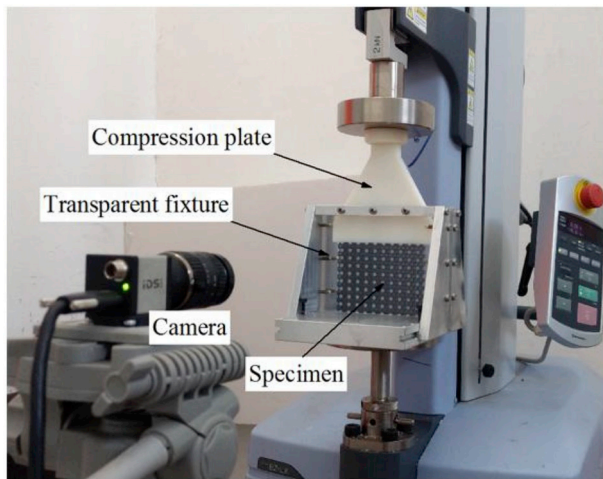


Fig. 2. Experimental setup.

where  $\mu$  and  $\Lambda$  denote the initial shear modulus and the first Lamé constant, respectively.  $I_1 = \text{tr}(\mathbf{F}^T \mathbf{F})$  and  $J = \det(\mathbf{F})$ , with  $\mathbf{F}$  denoting the deformation gradient. The high ratio  $\Lambda/\mu = 1000$  is used to maintain the nearly incompressible behavior of the material; for the soft matrix material the initial shear modulus is  $\mu^{(m)} = 0.6$  MPa. The inclusion-to-matrix ratio of shear moduli is chosen as  $\mu^{(i)}/\mu^{(m)} = 10^3$  so that the stiff inclusions almost do not deform.

To identify the onset of instability in infinite periodic composite under large deformations, Bloch-Floquet analysis superimposed on the deformed state is used [25,26,28,34,39,40]. The analysis is implemented in the nonlinear finite element code COMSOL 5.2a. To obtain the solution for the deformed state, we first apply the averaged macroscopic deformation through imposing periodic displacement boundary conditions on the edges of the primitive unit cell via  $\mathbf{u}_B - \mathbf{u}_A = (\bar{\mathbf{F}} - \mathbf{I})(\mathbf{X}_B - \mathbf{X}_A)$ , where  $\mathbf{X}$  denotes the position vector in the undeformed configuration;  $\mathbf{u}$  denotes the displacement vector;  $\bar{\mathbf{F}}$  is the applied macroscopic deformation gradient;  $A$  and  $B$  are the paired nodes periodically located at the opposite edges of the primitive unit cell. Then, Bloch-Floquet conditions are superimposed on the edges of the deformed primitive unit cell via  $\mathbf{u}(\mathbf{X} + \mathbf{R}) = \mathbf{u}(\mathbf{X})e^{-i\mathbf{K} \cdot \mathbf{R}}$ , where  $\mathbf{R}$  defines the distance between the paired nodes on the opposite edges of the unit cell;  $\mathbf{K}$  is the wave vector. Through gradually increasing the applied deformation along the loading path and solving the corresponding eigenvalue problem, the microscopic instability is identified, when the lowest eigenvalue (of a non-trivial eigenmode) attains zero. The corresponding applied strain level and wavenumber are identified as the critical strain  $\varepsilon^{cr}$  and critical wavenumber  $\mathbf{K}^{cr}$ . Note that macroscopic instability is detected when  $\mathbf{K}^{cr} \rightarrow 0$ ; this long wave instabilities can be identified through examining the loss of ellipticity analysis, and the corresponding conditions for the effective acoustic tensor or tensor of the elastic moduli [39,40]. Once the critical conditions are identified, the postbuckling analysis is performed. To this end, an updated unit cell is constructed – defined through the obtained critical wavenumber  $\mathbf{K}^{cr}$ . To trigger the instability induced pattern transformations, small amplitude imperfections in the form of the buckling mode (obtained from Bloch-Floquet instability analysis) are introduced in the initial geometry of the updated unit cell.

Quadratic triangular plane strain elements are used in simulations for periodic structures and finite size structures; a mesh sensitive analysis has been performed, in accordance to the analysis, mesh density of approximately 4000 elements for each primitive unit cell has been used.

In addition, numerical simulations on finite size specimens are conducted using explicit nonlinear finite element code LS-DYNA. The mesh of finite size structure is disturbed by introducing a small amplitude imperfection in the form of the first buckling mode obtained by linear

buckling analysis. In the analysis, the displacement of the top and bottom edges of the structure was constrained to be horizontally fixed. The contact between the edges for the collapsed voids is modeled using the CONTACT\_AUTOMATIC\_SINGLE\_SURFACE option. The quasi-static loading conditions are maintained while monitoring the force response and deformation mode being independent of the loading rate.

#### 4. Results and discussions

We start with studying of the deformation processes of the two types of the periodic composites *A* (as shown in Fig. 1(a)) and *B* (as shown in Fig. 1(b)) with a fixed volume fraction of the phases; next, we will examine the effect of the constituent volume fractions on the performance of the multiphase composites. Since the materials exhibit anisotropic behavior, we show their responses for different loading directions; in particular, each of the composite is tested under uniaxial compression in *X*- and *Y*-material directions. Fig. 3 shows the experimental and numerical results on deformation sequences for the composites at different deformation levels (the numerical results for infinite periodic and finite size specimens are given at the first and third rows, respectively; the experimental results are given at the second row). When the critical strain is reached, the voids collapse as the ligaments between them buckle. This leads to sudden microstructure transformations along with the breakage of composite symmetry and/or periodicity (see Fig. 3(a–d) at  $\varepsilon = 0.10$ ). As the deformation level is further increased, the instability-induced new patterns are rapidly accentuated (see Fig. 3(a–d) at  $\varepsilon = 0.15$ ) and start evolving. Remarkably, the significant lateral contraction with respect to the loading direction is observed both experimentally and numerically for all cases (see Fig. 3(a–d) at  $\varepsilon = 0.20$ ). This instability-induced negative Poisson's ratio or auxetic behavior is attributed to the microstructure transformation in the postbuckling regime. We note that the numerical simulations of the finite size samples nicely capture the boundary effects relevant to the experimental testing; due to the boundary effects only the central part of the specimens exhibit a nearly uniform deformation of the unit cells corresponding to the numerically modeled infinite periodic structures.

Moreover, both experiments and simulations show that the buckled patterns for *composite A* (with the square periodicity of inclusion distribution) loaded either in *X*- or *Y*-material directions consist of  $1 \times 2$  primitive unit cell; while *composite B* (with the triangular periodicity of inclusion distribution) preserves its initial periodicity even after the onset of instability for both loading directions. Moreover, thanks to the anisotropy of the composite microstructures, the development of the buckling patterns can be tuned by altering the loading direction. For example, different pattern developments are observed for *composite A* loaded in *X*- and *Y*-material directions; as a result, different effective behaviors can be observed for these loading cases, in particular, *composite A* loaded in *Y*-material direction exhibits a more significant lateral contraction behavior. Thus, this illustrates that rich pattern transformations can be obtained through tuning the positions of stiff inclusions and loading directions. Finally, the initial microstructure of the composites is fully recovered after the release of applied loading, demonstrating that these instability-induced pattern transformations are fully reversible.

Fig. 4 shows the experimental and numerical results of the evolution of nominal stress as functions of applied strain. The dotted vertical lines refer to the critical strains of the corresponding infinite periodic composites. We observe that the buckling strain is significantly influenced by the positions of stiff inclusions and loading directions. The critical strains for *composite A* loaded in *X*- and *Y*-material directions are  $\varepsilon_{cr} = 0.016$  and  $0.026$ , respectively; while the critical strains for *composite B* loaded in *X*- and *Y*-material directions are  $\varepsilon_{cr} = 0.062$  and  $0.048$ , respectively. Prior to the onset of instability, the stress-strain relation is characterized by an initial nearly linear behavior of the curves; in this stable regime, *composite A* has a larger effective modulus as compared to the response of *composite B*, regardless of the loading direction. We note



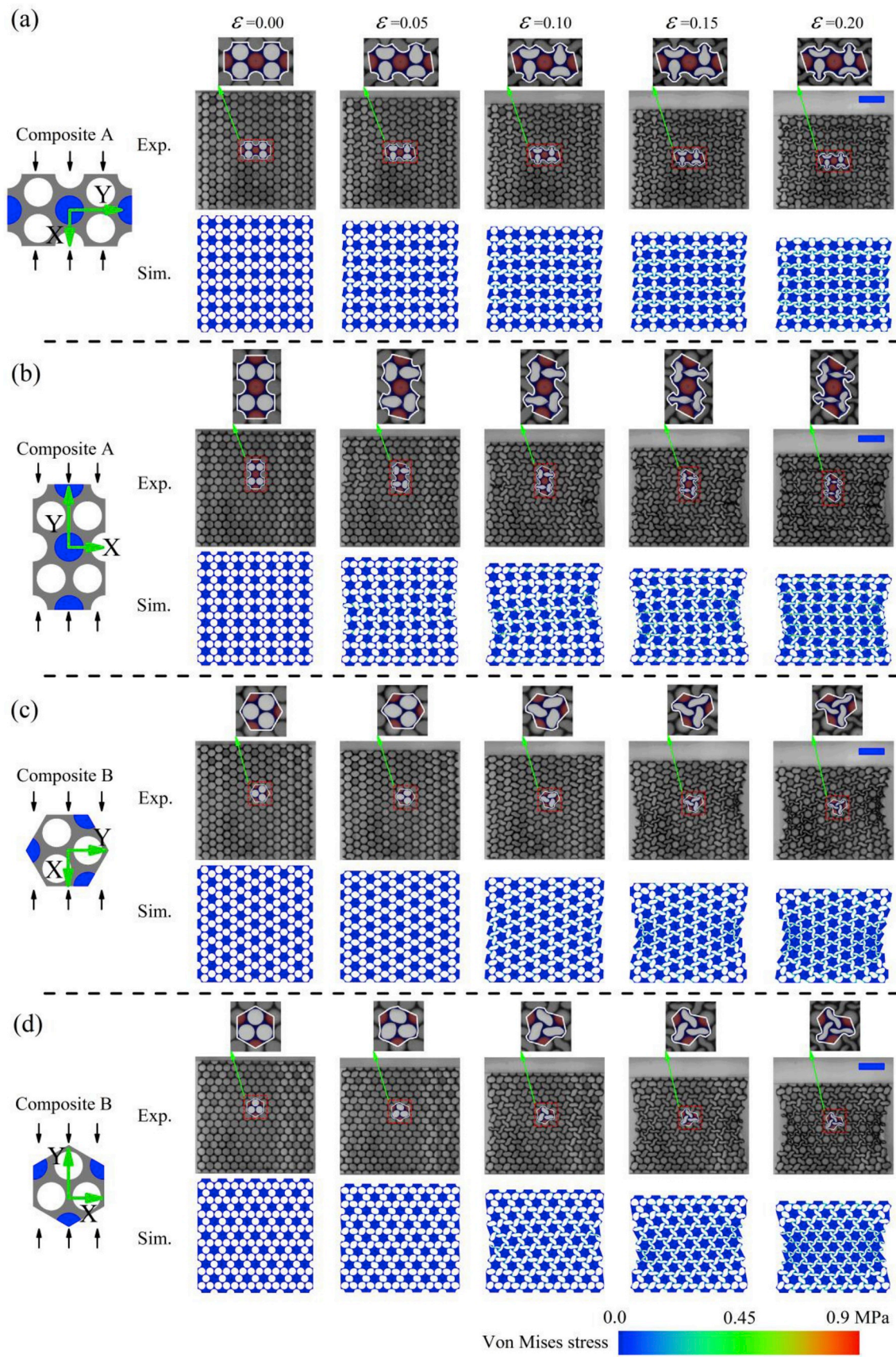


Fig. 3. Deformation sequences in soft composites at different deformation levels. Scale bar: 20 mm.

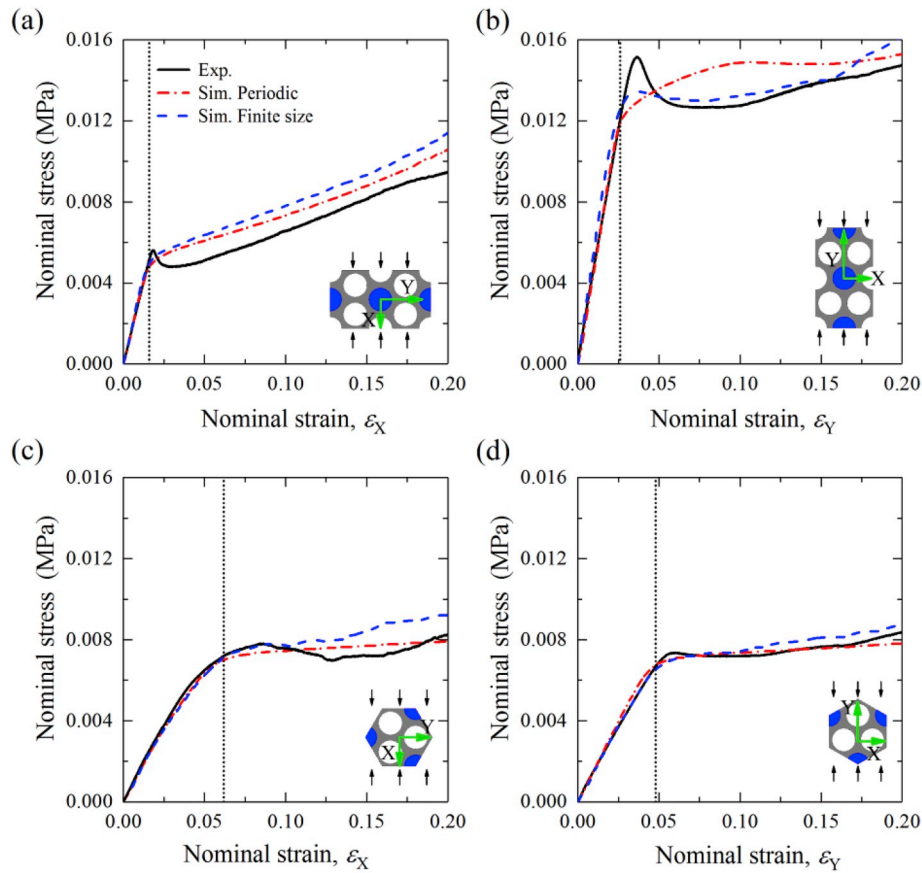


Fig. 4. Experimental and numerical stress-strain curves. Dotted lines denote critical strains for infinite periodic composites.

the agreement between the stress-strain curves observed in experiments and predicted by the finite element modeling for both finite size and infinite periodic structures. This is due to the fact that in the stable regime, each primitive unit cell undergoes a nearly identical deformation, which has been observed experimentally (see, for example, Fig. 3 (c) and (d) at  $\varepsilon = 0.05$ ). However, upon achieving the critical strain, softening behavior is observed in all cases due to development of elastic instability. We observe that *composites A* exhibits almost linear stress-strain curve behavior after buckling (for both loading directions); while for *composite B*, a plateau stress is observed following the onset of instabilities; this continues until the development of new patterns results in partial closure of the voids resulting in the increased overall stiffness. We note that a drop in the stress value is observed in the experiment after the applied deformation exceeds a critical level; this is more visible for *composite A* loaded in X- and Y-material directions; this phenomenon, however, is not captured by simulations. Similar differences between simulations and experiments were also reported in the system of periodic elastomeric array of circular voids [43]. There is a number of factors – stemming from the numerical model simplifications – that may contribute to the observed differences. These include the constitutive material model with the absence of inelastic behavior, strong plane strain constrain, absence of friction, and possible dynamic effects not accounted for in the numerical simulations.

Fig. 5 shows the dependence of the effective Poisson's ratio on the applied strain. The blue dashed and red dash-dotted curves correspond to the numerical results for finite size and infinite periodic structures, respectively; while the experimental results are denoted by the black

points with error bar<sup>1</sup> symbols (the details about calculation of the effective Poisson's ratio are given in the Appendix). We observe a good agreement between the trends of the curves for numerical results and experimental observations; however, some quantitative differences are observed, especially in the initial regime of relatively small deformations. In this regime, the displacement of stiff inclusion is relatively small, and the measurement inaccuracy influences the calculated value of the effective Poisson's ratio. After the applied deformation exceeds the critical strain, due to the buckling of the ligaments resulting in void collapse, a rapid drop in Poisson's ratio up to a negative regime is observed in both experiments and simulations for all cases. The drop in Poisson's ratio is followed by a slow decrease with a further increase in the applied deformation. While for *composite A* loaded in X-material direction excellent agreement between experiments and simulations is observed, for other cases, the simulations on finite size structures show a better agreement with experiments in comparison to the results from the simulations of the infinite periodic structures. This is due to the fact that the finite size specimen (of *composite A* loaded in X-material direction) exhibits nearly identical deformation of the unit cells up to  $\varepsilon = 0.2$  (see Fig. 3(a)). For other cases (*Composite A* loaded in Y-material direction, and *composite B* loaded in X- and Y-material directions), the lateral edges of the specimens significantly bend inward due to the strong negative Poisson's ratio behavior (see Fig. 3(b–d) at  $\varepsilon = 0.2$ ); this effect is not accounted for in the infinite periodic structure simulations. Finally, we note the significant dependence of the instability-induced negative Poisson's ratio behavior on the positions of stiff inclusions and loading directions. For example, at applied strain  $\varepsilon = 0.2$ , effective Poisson's

<sup>1</sup> The error bars represent the standard deviations of the calculated effective Poisson's ratio values based on various selected representative elements; the calculation procedure is described in the Appendix.



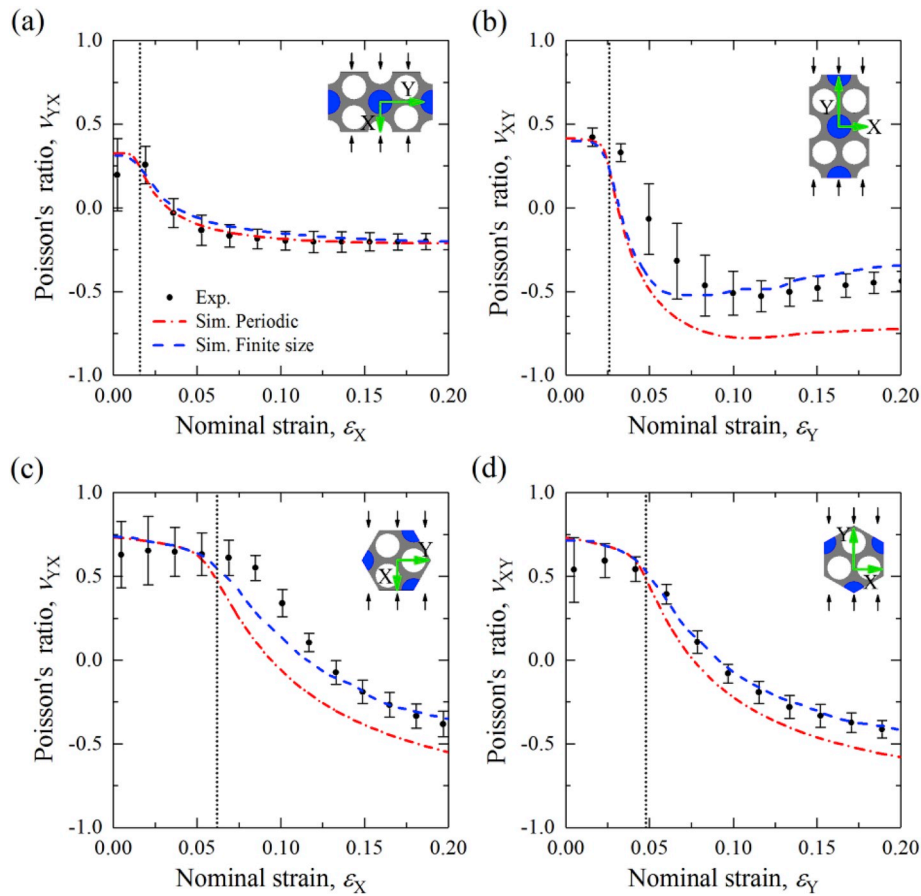


Fig. 5. Effective Poisson's ratio vs strain level.

ratios for infinite periodic *composite A* loaded in X- and Y-material directions are  $\nu_{YX} = -0.21$  and  $\nu_{XY} = -0.72$ , respectively; while the Poisson's ratios for infinite periodic *composite B* loaded in X- and Y-material directions are  $\nu_{YX} = -0.55$  and  $\nu_{XY} = -0.58$ , respectively.

For completeness, we show the effect of the inclusion distribution and loading direction on the initial responses (in the stable regime of small deformations) of the periodic composites. Fig. 6 presents the dependence of effective Young's modulus and Poisson's ratio on inclusion volume fraction for the composites with various void volume fractions. The dashed curves with markers and the continuous curves refer to the results of the composite loaded in X- and Y-material directions, respectively. The effective Young's modulus is calculated as  $E^{\text{eff}} = 2U\varepsilon^{-2}/A$ , where  $U$  is the stored elastic energy;  $A$  is the area of the primitive unit cell;  $\varepsilon$  is the applied strain. The method has been verified against the analytical estimation for inclusion-reinforced composite with stiff inclusions periodically embedded in a softer matrix arranged in a hexagonal array [57]. The effective Young's modulus is normalized as  $\tilde{E} = E^{\text{eff}}/\mu^{(m)}$ . We observe that the effective Young's modulus and Poisson's ratio for *composite A* loaded in X- and Y-material directions are clearly different (see Fig. 6(a) and (c)); whereas the corresponding responses for *composite B* loaded in X- and Y-material directions are identical (see Fig. 6(b) and (d)). *Composite A* shows a stiffer response when loaded in Y-material as compared to its response to loading in X-direction. For both cases, an increase in inclusion volume fraction leads to an increase in effective Young's modulus, and this effect is more significant for the composite with smaller void volume fraction. For example, an increase in stiff volume fraction of *composite B* from  $c^{(i)} = 0.05$  to 0.25 results an increase in effective Young's modulus from  $\tilde{E} = 0.148$  to 0.160 for the case  $c^{(v)} = 0.6$ , from  $\tilde{E} = 2.288$  to 2.832 for the case  $c^{(v)} = 0.2$ . Larger Poisson's ratios are observed for *composite A*

loaded in Y-material direction in comparison to the load in X-material direction; and composites with higher inclusion volume fractions exhibit lower Poisson's ratios (see Fig. 6(c)). The effect of inclusion volume fraction on Poisson's ratio in *composite B* is very different, and it strongly depends on the composite void volume fraction (see Fig. 6(d)). For instance, the influence of inclusion volume fraction on Poisson's ratio for *composite B* with  $c^{(v)} = 0.6$  is negligible; whereas an increase in inclusion volume fraction results in a significant decrease in Poisson's ratio for *composite B* with  $c^{(v)} = 0.3$ .

Next, we examine the influence of the phase volume fractions on the onset of instabilities. To this end, we perform the Bloch-Floquet analysis (described in the Numerical Modeling Section). Fig. 7 shows the dependence of critical strain on the composite matrix volume fraction. Here, the radii of the circular voids and stiff inclusions are set to be identical. Note that in the considered range  $c^{(v)} \in (0.2, 0.4)$ , all composites experience microscopic instabilities, and the buckling mode of *composite A* consists of  $1 \times 2$  primitive unit cell, while *composite B* preserves its initial  $1 \times 1$  periodicity (see Fig. 1). Regardless of the positions of the stiff inclusions and loading directions, we observe that a decrease in matrix volume fraction results in an earlier onset of instability. This is because the composites with lower matrix volume fractions has slender ligaments that are prone to buckling. We observe that *composite A* loaded in X-direction buckles earlier as compared to the response in Y-direction; whereas *composite B* is more stable when the applied load is in X-material direction. Moreover, we note that *composite A* is more prone to buckling than *composite B* for both loading directions.

Fig. 8 shows the evolution of Poisson's ratio with applied compressive strain for composites with various matrix volume fractions (with the radii of circular voids and stiff inclusions set to be identical). We note that, prior to the onset of instability, Poisson's ratio is positive for all

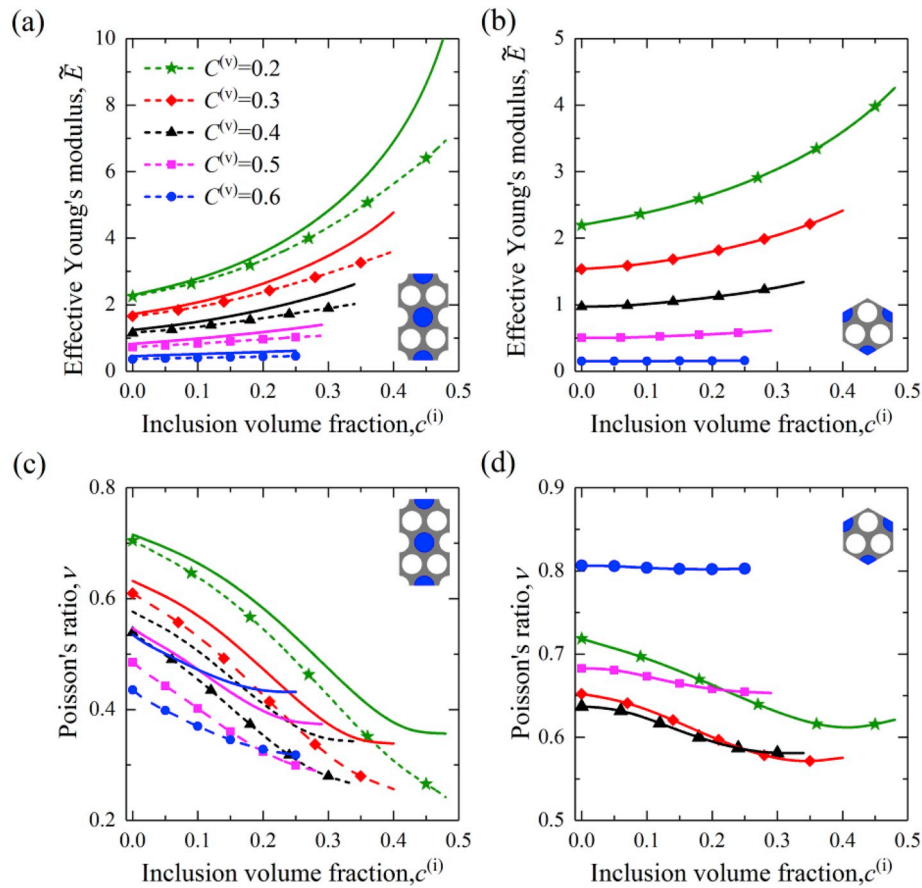


**Fig. 6.** Dependence of effective Young's modulus and Poisson's ratio on inclusion volume fraction for composites with various void volume fractions in the stable regime of small deformations. The dashed curves with markers and the continuous curves refer to the results of the composite loaded in X- and Y-material directions, respectively.

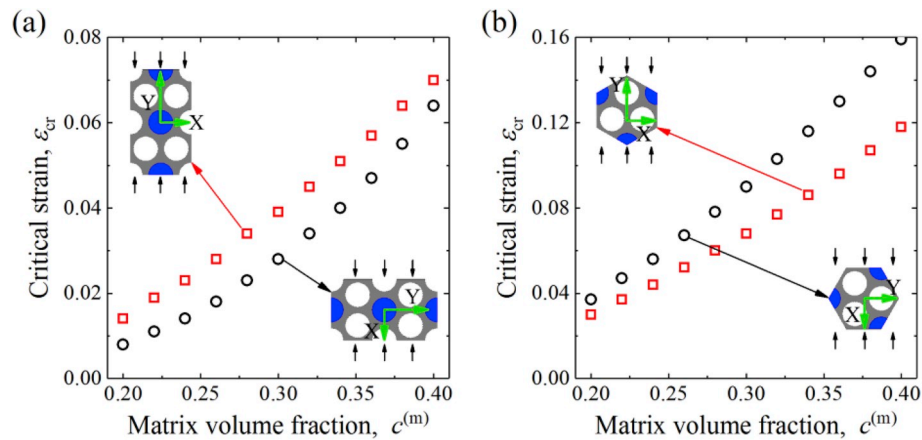


**Fig. 7.** Dependence of critical strain on matrix volume fraction. The radii of circular voids and stiff inclusions are identical.

considered cases. However, upon onset of instabilities and microstructure transformations, an increase in deformation results in a dramatic drop in Poisson's ratio down to the negative regime. The analysis shows that a stronger auxetic or negative Poisson's ratio behavior can be obtained through decreasing the matrix volume fraction (i.e., increasing the void volume fraction). Remarkable, for *composite A* loaded in X-material direction, the value of negative Poisson's ratio for the composite with lower matrix volume fraction is found to be nearly independent on applied strain after a certain deformation level. For instance, for *composite A* with  $c^{(m)} = 0.2$ , Poisson's ratio is nearly constant at

$\nu_{YX} \approx -0.21$  when applied strain  $\varepsilon_X \geq 0.08$ . When *composite A* loaded in Y-material direction, we observe that Poisson's ratio for the case  $c^{(m)} = 0.2$  can attain extreme values, for example,  $\nu_{XY} = -0.99$  at the applied strain  $\varepsilon_Y = 0.07$ ; however, this minimum is followed by an increase in Poisson's ratio with further increase in the applied deformation. For *composite B*, we observe similar trends for loadings in X- and Y-material directions, especially for the composites with small matrix volume fractions.

Furthermore, we examine the influence of the inclusion volume fraction on the composite behavior, while keeping the void volume

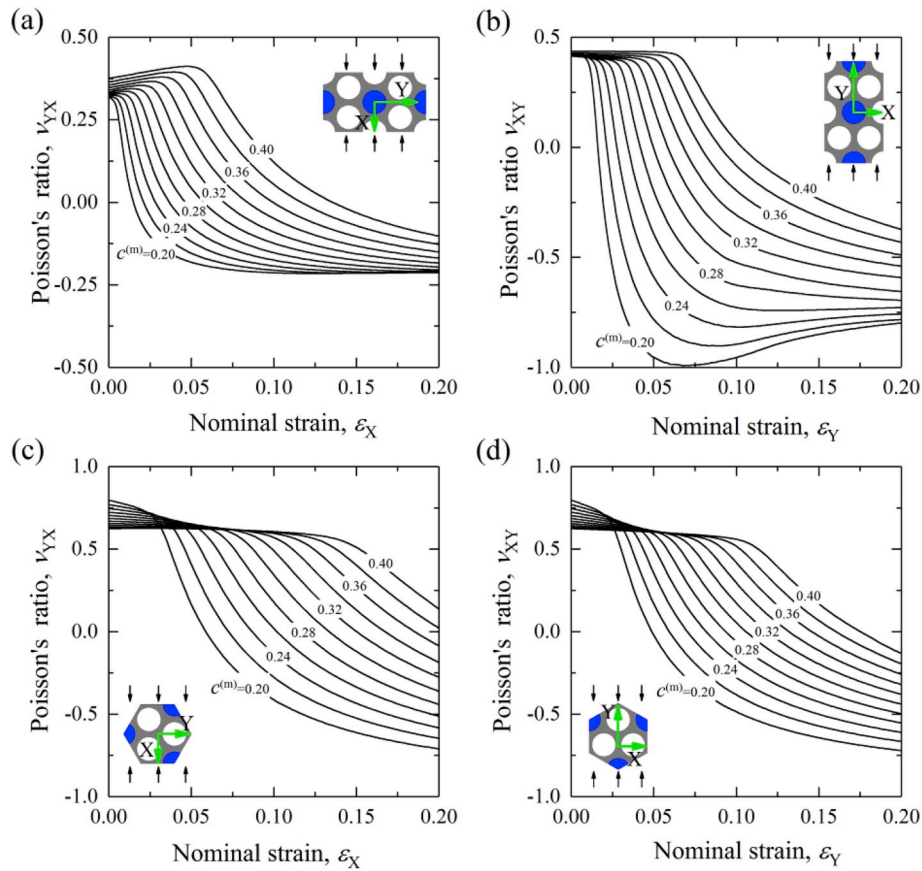


**Fig. 8.** Dependence of Poisson's ratio on applied deformation for composites with various matrix volume fractions. The radii of voids and stiff inclusions are identical.

fraction fixed. Fig. 9 shows the dependence of the critical strain and Poisson's ratio on the inclusion volume fraction. The void volume fraction is fixed as  $c^{(v)} = 0.45$  and Poisson's ratio is evaluated at  $\varepsilon = 0.2$ . Composites with larger stiff inclusions are compared to buckle earlier for all considered cases. Thus, a larger negative value of Poisson's ratio can be achieved at the same level of deformation by increasing the stiff inclusion volume fraction. For example, for *composite A* loaded in Y-material direction, an increase in the stiff inclusion volume fraction from  $c^{(i)} = 0.0$  to 0.3 leads to a decrease in Poisson's ratio from  $\nu_{XY} = -0.22$  to  $-0.55$ . In *composite B* loaded in X-material direction, a change in the stiff inclusion volume fraction has a more significant influence on the buckling strain and Poisson's ratio in comparison to the composite loaded in Y-direction (compare Fig. 9(c) and (d)). Moreover, it is notable that the effect of the inclusion volume fraction on the buckling strain and Poisson's ratio behavior can be stronger for composites with smaller radius of voids.

Finally, we investigate the role of shear modulus contrast on the soft composite behavior. Fig. 10 shows the dependence of critical strain and Poisson's ratio on shear modulus contrast. The matrix volume fraction is fixed as  $c^{(m)} = 0.65$  and the radii of voids and stiff inclusions are identical. Poisson's ratio is evaluated at  $\varepsilon = 0.2$ . Note that, for the considered range  $\mu^{(i)}/\mu^{(m)}$  from 1 to  $10^4$ , *composite A* buckles and forms the new periodicity consisted of  $1 \times 2$  primitive unit cell, while *composite B* preserves its initial periodicity for both loading directions. We observe that the composite with a higher shear modulus contrast buckles earlier, resulting in a more significant negative Poisson's ratio behavior. However, when the contrast  $\mu^{(i)}/\mu^{(m)}$  is larger than  $10^3$ , this effect becomes negligible. We note that a change in  $\mu^{(i)}/\mu^{(m)}$  has more significant influence on the critical strain and Poisson's ratio for the case of *composite A* loaded in Y-material direction (see Fig. 10 (b)). For example, an

increase in the contrast  $\mu^{(i)}/\mu^{(m)}$  from 1 to  $10^3$  can result in a decrease in critical strain from  $\varepsilon_{cr} = 0.075$  to 0.054, and a decrease in Poisson's ratio from  $\nu_{XY} = -0.397$  to  $-0.515$ . For the case of *composite B*, the composite loaded in X-material direction is more sensitive to a change in shear modulus contrast in comparison to the composite loaded in Y-material direction (compare Fig. 10 (c) with (d)).

## 5. Conclusions

We have investigated the instability-induced pattern transformations in multiphase composites consisted of circular voids and stiff inclusions periodically distributed in a soft elastomer. In this study, we specifically focused on the role of inclusion distribution and anisotropic property on the mechanical responses of the composites. We studied two types of stiff inclusion arrangements in the porous structure comprising of a triangular array of circular voids, where elastic instability can be exploited to trigger cooperative buckling of voids. Through the combination of simulations and experiments on the 3D printed composites, we have realized multiple new patterns. We showed that these new patterns can be tuned by altering the distribution of stiff inclusions, thus, switchable extremely soft and negative Poisson's ratio behavior can be tailored.

Furthermore, through the survey of the microstructure parameter space, we provide the trends for the changes in the effective properties as functions of the microstructure parameters. We have found that the composites may attain extreme values of negative Poisson's ratio for certain morphologies and loadings. Thus, the composites with square periodic arrangement of the stiff inclusions (*composite A*) with low matrix volume fractions have been identified as the advantageous configurations with high tunability of the effective properties by deformation. Moreover, the tailored composite morphologies allow to pre-design the



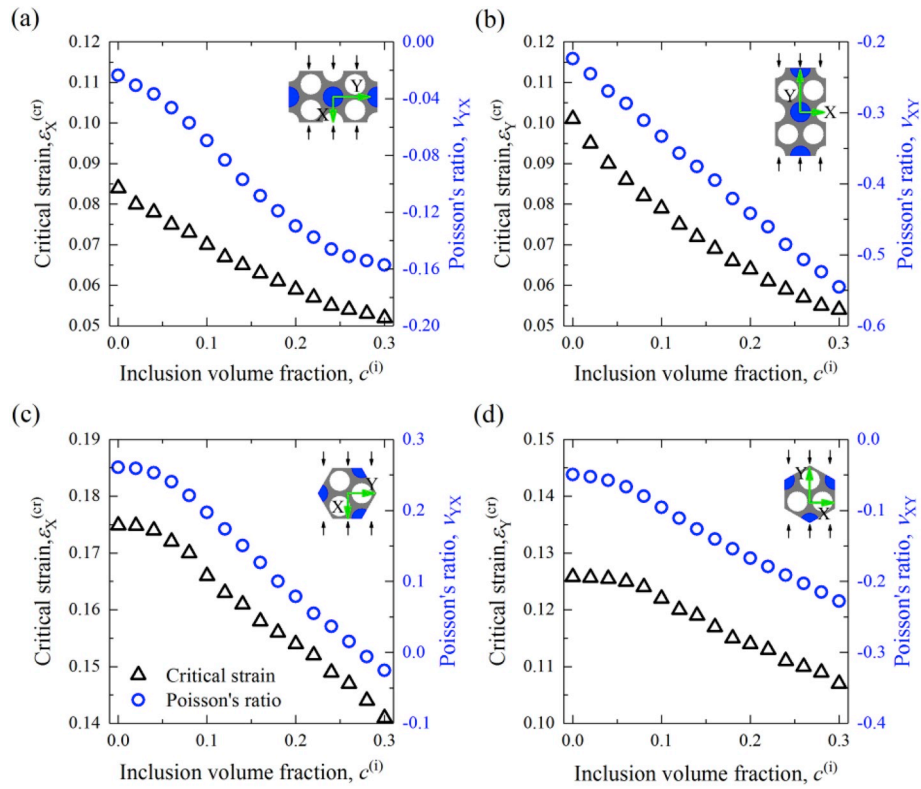


**Fig. 9.** Dependence of critical strain and Poisson's ratio on inclusion volume fraction. Void volume fraction is fixed as  $c^{(v)} = 0.45$ . Poisson's ratio is evaluated at deformation level of  $\varepsilon = 0.2$ .

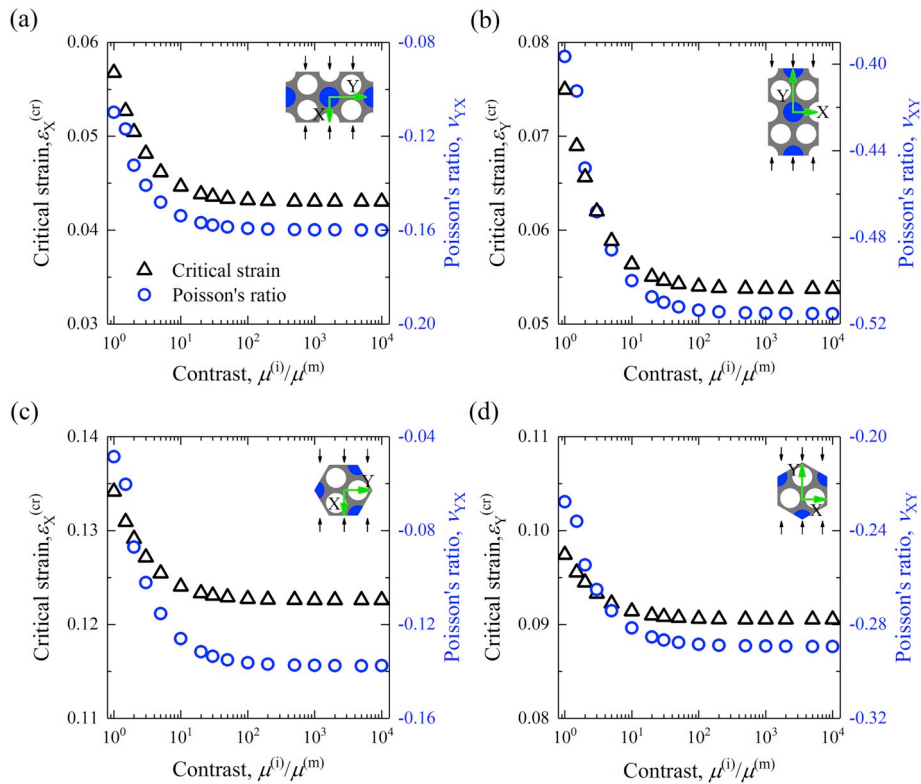


**Fig. 10.** Dependence of critical strain and Poisson's ratio on shear modulus contrast  $\mu^{(i)}/\mu^{(m)}$ . The matrix volume fraction is fixed as  $c^{(m)} = 0.65$ . The radii of voids and stiff inclusions are identical. Poisson's ratio is evaluated at the deformation level of  $\varepsilon = 0.2$ .

onset of instabilities. Thus, we have found that the composites with larger void and/or stiff inclusion volume fractions, as well as a higher inclusion-to-matrix ratio of shear moduli, are more prone to buckling, and, hence, they exhibit a more pronounced negative Poisson's ratio behavior. The composites with the square periodic inclusion arrangement (*composite A*) are more stable in comparison to the composites with the triangular periodic inclusion arrangement (*composite B*). Thus, the performance of the composites can be significantly tuned via altering the distribution of stiff inclusions, loading directions, phase volume fractions, and shear modulus contrast. The reported behavior of the soft microstructures can be potentially used in designing materials for energy dissipation and shock wave mitigation; vibration and noise management, and novel soft actuators with morphing abilities. These actuators can incorporate functionalized inclusions to respond to applied electrical [58] or magnetic field [5,59], potentially enabling

future design of actively and/or remotely controlled functional materials. Finally, we note that – since the overall response of these materials is highly compressible, and even exhibiting auxetic behavior in the postbuckling regimes – the response to unidirectional tensile loadings may result in different behavior as compared to the compressive loading considered here. The effect of various loading conditions, such as tensile or bi-axial loadings, can be exploited to gain access to distinct pattern transformations, and, potentially, different behavior in the postbuckling regime [55,60–62].

### Acknowledgements

This work was supported by the Israel Science Foundation (Grant No. 1550/15 and 1973/15). J. L. acknowledges the support from Lady Davis Fellowship.

### Appendix. Calculation of the effective Poisson's ratio

Here we describe the procedure for calculating the effective Poisson's ratio based on the experimental testing. In experiments, the deformation process was recorded by a high-resolution digital camera producing a sequence of frames at increasing strain levels. The position for the centroid of each circular stiff inclusion, marked by black dot, is tracked through the digital image analysis of the recorded frames. To diminish the boundary effect, we focus on the central part of the finite size specimens, where more uniform deformation is observed for each updated unit cell. The selected areas for the tested specimens are highlighted in green color in Fig. A1(b–e). The selected representative elements and stiff inclusions are numbered by their row and column indices. The applied strain for representative element is calculated as

$$\varepsilon_{XX}^{[i,j]} = \frac{x^{(i,j+1)} - x^{(i,j)} + x^{(i+1,j+1)} - x^{(i+1,j)} - 2L_X^0}{2L_X^0} \quad (A1)$$

$$\varepsilon_{YY}^{[i,j]} = \frac{y^{(i+1,j)} - y^{(i,j)} + y^{(i+1,j+1)} - y^{(i,j+1)} - 2L_Y^0}{2L_Y^0} \quad (A2)$$

where  $L_X^0$  and  $L_Y^0$  are defined in undeformed state, given in Fig. A1(a). The Poisson's ratios for the considered representative element  $[i, j]$  when loaded in X- and Y-material directions are calculated as

$$\nu_{YX}^{[i,j]} = -\frac{\varepsilon_{YY}^{[i,j]}}{\varepsilon_{XX}^{[i,j]}} \quad (A3)$$

$$\nu_{XY}^{[i,j]} = -\frac{\varepsilon_{XX}^{[i,j]}}{\varepsilon_{YY}^{[i,j]}} \quad (A4)$$

Finally, the effective Poisson's ratio is given as the averaged value for nine selected representative elements.

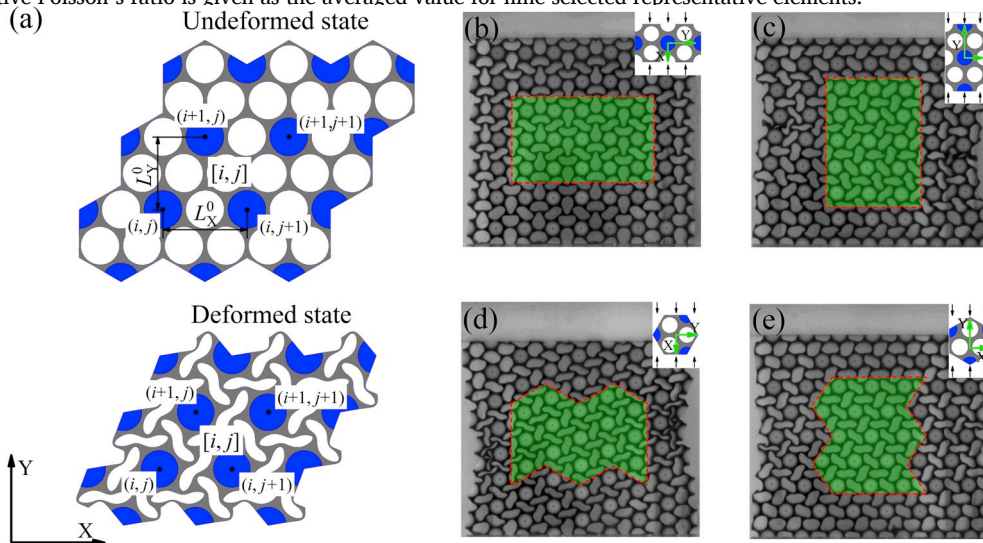


Fig. A1. Schematic diagrams (a) and selected areas (b–e) for calculation of the effective Poisson's ratio.

## References

- [1] Lau K, Hung PY, Zhu MH, Hui D. Properties of natural fibre composites for structural engineering applications. *Compos B Eng* 2018;136:222–33.
- [2] Compton BG, Lewis JA. 3D-Printing of lightweight cellular composites. *Adv Mater* 2014;26:5930–5.
- [3] Mohan VB, Lau K, Hui D, Bhattacharyya D. Graphene-based materials and their composites: a review on production, applications and product limitations. *Compos B Eng* 2018;142:200–20.
- [4] Scarponi C, Messano M. Comparative evaluation between E-Glass and hemp fiber composites application in rotorcraft interiors. *Compos B Eng* 2015;69:542–9.
- [5] Goshkoderia A, Rudykh S. Stability of magnetoactive composites with periodic microstructures undergoing finite strains in the presence of a magnetic field. *Compos B Eng* 2017;128:19–29.
- [6] Yuan C, Mu X, Dunn CK, Haidar J, Wang T, Jerry Qi H. Thermomechanically triggered two-stage pattern switching of 2D lattices for adaptive structures. *Adv Funct Mater* 2018;28:1705727.
- [7] Cho H, Weaver JC, Pösel E, in't Veld PJ, Boyce MC, Rutledge GC. Engineering the mechanics of heterogeneous soft crystals. *Adv Funct Mater* 2016;26:6938–49.
- [8] Che K, Yuan C, Wu J, Jerry Qi H, Meaud J. Three-dimensional-printed multistable mechanical metamaterials with a deterministic deformation sequence. *J Appl Mech* 2016;84, 011004.
- [9] Che K, Yuan C, Qi HJ, Meaud J. Viscoelastic multistable architected materials with temperature-dependent snapping sequence. *Soft Matter* 2018;14:2492–9.
- [10] Gutttag M, Boyce MC. Locally and dynamically controllable surface topography through the use of particle-enhanced soft composites. *Adv Funct Mater* 2015;25: 3641–7.
- [11] Rafsanjani A, Akbarzadeh A, Pasini D. Snapping mechanical metamaterials under tension. *Adv Mater* 2015;27:5931–5.
- [12] Kochmann DM, Bertoldi K. Exploiting microstructural instabilities in solids and structures: from metamaterials to structural transitions. *Appl Mech Rev* 2017;69, 050801.
- [13] Meaud J, Che K. Tuning elastic wave propagation in multistable architected materials. *Int J Solids Struct* 2017;122(123):69–80.
- [14] Herrmann LR, Mason WE, Chan STK. Response of reinforcing wires to compressive states of stress. *J Compos Mater* 1967;1:212–26.
- [15] Parnes R, Chiskis A. Buckling of nano-fibre reinforced composites: a re-examination of elastic buckling. *J Mech Phys Solids* 2002;50:855–79.
- [16] Andrianov IV, Kalamkarov AL, Weichert D. Buckling of fibers in fiber-reinforced composites. *Compos B Eng* 2012;43:2058–62.
- [17] Ogden RW. Non-linear elastic deformations. New York: Dover Publications; 1997.
- [18] Merodio J, Ogden RW. Material instabilities in fiber-reinforced nonlinearly elastic solids under plane deformation. *Arch Mech* 2002;54:525–52.
- [19] Merodio J, Ogden RW. Instabilities and loss of ellipticity in fiber-reinforced compressible non-linearly elastic solids under plane deformation. *Int J Solids Struct* 2003;40:4707–27.
- [20] Merodio J, Ogden RW. Mechanical response of fiber-reinforced incompressible non-linearly elastic solids. *Int J Non-Linear Mech* 2005;40:213–27.
- [21] Merodio J, Ogden RW. Remarks on instabilities and ellipticity for a fiber-reinforced compressible nonlinearly elastic solid under plane deformation. *Q Appl Math* 2005; 63:325–33.
- [22] Rudykh S, DeBotton G. Instabilities of hyperelastic fiber composites: micromechanical versus numerical analyses. *J Elast* 2012;106:123–47.
- [23] Li J, Pallicity TD, Slesarenko V, Goshkoderia A, Rudykh S. Domain formations and pattern transitions via instabilities in soft heterogeneous materials. *Adv Mater* 2019;31:1807309.
- [24] Nestorović MD, Triantafyllidis N. Onset of failure in finitely strained layered composites subjected to combined normal and shear loading. *J Mech Phys Solids* 2004;52:941–74.
- [25] Bertoldi K, Boyce MC. Wave propagation and instabilities in monolithic and periodically structured elastomeric materials undergoing large deformations. *Phys Rev B* 2008;78:184107.
- [26] Slesarenko V, Rudykh S. Microscopic and macroscopic instabilities in hyperelastic fiber composites. *J Mech Phys Solids* 2017;99:471–82.
- [27] Li J, Slesarenko V, Galich PI, Rudykh S. Instabilities and pattern formations in 3D-printed deformable fiber composites. *Compos B Eng* 2018;148:114–22.
- [28] Li J, Slesarenko V, Rudykh S. Microscopic instabilities and elastic wave propagation in finitely deformed laminates with compressible hyperelastic phases. *Eur J Mech/A Solids* 2019;73:126–36.
- [29] Galich PI, Slesarenko V, Li J, Rudykh S. Elastic instabilities and shear waves in hyperelastic composites with various periodic fiber arrangements. *Int J Eng Sci* 2018;130:51–61.
- [30] Tang Y, Lin G, Han L, Qiu S, Yang S, Yin J. Design of hierarchically cut hinges for highly stretchable and reconfigurable metamaterials with enhanced strength. *Adv Mater* 2015;27:7181–90.
- [31] Mizzi L, Azzopardi KM, Attard D, Grima JN, Gatt R. Auxetic metamaterials exhibiting giant negative Poisson's ratios. *Phys Status Solidi Rapid Res Lett* 2015;9: 425–30.
- [32] Wang P, Shim J, Bertoldi K. Effects of geometric and material nonlinearities on tunable band gaps and low-frequency directionality of phononic crystals. *Phys Rev B* 2013;88, 014304.
- [33] Shan S, Kang SH, Wang P, Qu C, Shian S, Chen ER, et al. Harnessing multiple folding mechanisms in soft periodic structures for tunable control of elastic waves. *Adv Funct Mater* 2014;24:4935–42.
- [34] Shim J, Wang P, Bertoldi K. Harnessing instability-induced pattern transformation to design tunable phononic crystals. *Int J Solids Struct* 2015;58:52–61.
- [35] Li J, Slesarenko V, Rudykh S. Auxetic multiphase soft composite material design through instabilities with application for acoustic metamaterials. *Soft Matter* 2018; 14:6171–80.
- [36] Li J, Shim J, Deng J, Overvelde JTB, Zhu X, Bertoldi K, et al. Switching periodic membranes via pattern transformation and shape memory effect. *Soft Matter* 2012; 8:10322.
- [37] Yang D, Mosadegh B, Ainla A, Lee B, Khashai F, Suo Z, et al. Buckling of elastomeric beams enables actuation of soft machines. *Adv Mater* 2015;27:6323–7.
- [38] Abeyaratne R, Triantafyllidis N. An investigation of localization in a porous elastic material using homogenization theory. *J Appl Mech* 1984;51:481–5.
- [39] Triantafyllidis N, Maker BN. On the comparison between microscopic and macroscopic instability mechanisms in a class of fiber-reinforced composites. *J Appl Mech* 1985;52:794.
- [40] Geymonat G, Müller S, Triantafyllidis N. Homogenization of nonlinearly elastic materials, microscopic bifurcation and macroscopic loss of rank-one convexity. *Arch Ration Mech Anal* 1993;122:231–90.
- [41] Triantafyllidis N, Nestorović MD, Schraad MW. Failure surfaces for finitely strained two-phase periodic solids under general in-plane loading. *J Appl Mech* 2006;73: 505–15.
- [42] Michel JC, Lopez-Pamies O, Ponte Castañeda P, Triantafyllidis N. Microscopic and macroscopic instabilities in finitely strained porous elastomers. *J Mech Phys Solids* 2007;55:900–38.
- [43] Mullin T, Deschanel S, Bertoldi K, Boyce MC. Pattern transformation triggered by deformation. *Phys Rev Lett* 2007;99, 084301.
- [44] Zhang Y, Matsumoto EA, Peter A, Lin P, Kamien RD, Yang S. One-step nanoscale Assembly of complex structures via harnessing of an elastic instability. *Nano Lett* 2008;8:1192–6.
- [45] Singamaneni S, Bertoldi K, Chang S, Jang JH, Thomas EL, Boyce MC, et al. Instabilities and pattern transformation in periodic, porous elastoplastic solid coatings. *ACS Appl Mater Interfaces* 2009;1:42–7.
- [46] Singamaneni S, Bertoldi K, Chang S, Jang JH, Young SL, Thomas EL, et al. Bifurcated mechanical behavior of deformed periodic porous solids. *Adv Funct Mater* 2009;19:1426–36.
- [47] Bertoldi K, Reis PM, Willshaw S, Mullin T. Negative Poisson's ratio behavior induced by an elastic instability. *Adv Mater* 2010;22:361–6.
- [48] Babaee S, Shim J, Weaver JC, Chen ER, Patel N, Bertoldi K. 3D soft metamaterials with negative Poisson's ratio. *Adv Mater* 2013;25:5044–9.
- [49] Bertoldi K, Boyce MC, Deschanel S, Prange SM, Mullin T. Mechanics of deformation-triggered pattern transformations and superelastic behavior in periodic elastomeric structures. *J Mech Phys Solids* 2008;56:2642–68.
- [50] Shim J, Shan S, Košmrlj A, Kang SH, Chen ER, Weaver JC, et al. Harnessing instabilities for design of soft reconfigurable auxetic/chiral materials. *Soft Matter* 2013;9:8198.
- [51] Overvelde JTB, Bertoldi K. Relating pore shape to the non-linear response of periodic elastomeric structures. *J Mech Phys Solids* 2014;64:351–66.
- [52] Overvelde JTB, Shan S, Bertoldi K. Compaction through buckling in 2D periodic, soft and porous structures: effect of pore shape. *Adv Mater* 2012;24:2337–42.
- [53] Florijn B, Coulaïs C, van Hecke M. Programmable mechanical metamaterials. *Phys Rev Lett* 2014;113:175503.
- [54] Florijn B, Coulaïs C, van Hecke M. Programmable mechanical metamaterials: the role of geometry. *Soft Matter* 2016;12:8736–43.
- [55] Overvelde JTB, Dykstra DMJ, de Rooij R, Weaver J, Bertoldi K. Tensile instability in a thick elastic body. *Phys Rev Lett* 2016;117, 094301.
- [56] Shim J, Perdigou C, Chen ER, Bertoldi K, Reis PM. Buckling-induced encapsulation of structured elastic shells under pressure. *Proc Natl Acad Sci Unit States Am* 2012; 109:5978–83.
- [57] Sun CT, Vaidya RS. Prediction of composite properties from a representative volume element. *Compos Sci Technol* 1996;56:171–9.
- [58] Yan J, Han M, Zhang J, Xu C, Luijten E, Granick S. Reconfiguring active particles by electrostatic imbalance. *Nat Mater* 2016;15:1095–9.
- [59] Ciambella J, Stanier DC, Rahatekar SS. Magnetic alignment of short carbon fibers in curing composites. *Compos B Eng* 2017;109:129–37.
- [60] Gao C, Slesarenko V, Boyce MC, Rudykh S, Li Y. Instability-induced pattern transformation in soft metamaterial with hexagonal networks for tunable wave propagation. *Sci Rep* 2018;8:11834.
- [61] Gao N, Li J, Bao R, Chen W. Harnessing uniaxial tension to tune Poisson's ratio and wave propagation in soft porous phononic crystals: an experimental study. *Soft Matter* 2019;15:2921–7.
- Gao N, Huang Y, Ronghao B, Chen W. Robustly tuning bandgaps in two-dimensional soft phononic crystals with criss-crossed elliptical holes. *Acta Mech Solida Sin* 2018;31: 573–88.